Astronomy and Computing 32 (2020) 100408

Contents lists available at ScienceDirect

Astronomy and Computing

journal homepage: www.elsevier.com/locate/ascom

Full length article

Space target extraction and detection for wide-field surveillance

D. Liu [a,b], X. Wang [a,*], Z. Xu [a,b], Y. Li [a], W. Liu [a]

[a] Changchun Institute of Optics, Fine Mechanics and Physics, Chinese Academy of Sciences, Changchun 130033, China
[b] University of Chinese Academy of Sciences, Beijing 100049, China

ARTICLE INFO

Article history:
Received 7 January 2020
Accepted 28 July 2020
Available online 1 August 2020

Keywords:
Space target detection
Wide-field space surveillance
Morphological filtering
Multistage hypothesis testing

ABSTRACT

A wide-field surveillance system with a long exposure time has a stronger capability of space target detection. However, it also produces some complicated situations that make it difficult to detect space targets; some stars appear as streak-like sources, countless object points, and possible discontinuous or nonlinear target trajectories. We present a space target detection method with high detection probability and low computational cost to overcome these obstacles. Firstly, the improved adaptive threshold method and the omnidirectional morphological filtering method are implemented to remove stars and noise. Secondly, the relative inter frame motion distance can be used as the basis for predicting the valid state transition region in each image. Finally, a state transition multistage hypothesis testing method is proposed to detect targets with linear, nonlinear, continuous or discontinuous trajectories. As demonstrated by the experimental results in simulated image sequences and real image sequences, the proposed algorithm can effectively detect space targets in wide-field surveillance with long exposure time, and has a high detection probability and low computational cost.

1. Introduction

The number of man-made targets in space has been increasing since Sputnik-1 was launched in 1957 (Castronuovo, 2011; Wirnsberger et al., 2015; Esmiller et al., 2014). Only a fraction of the detected targets are operational satellites, while the rest can be classified as space debris. Sixty years ago, space seemed to be infinite, but the space age has proven that the orbit around the earth can be filled up very quickly. Space targets pose a serious hazard to human space activities and properly functioning satellites (Nunez et al., 2015). In order to predict and avoid these threats, it is very important to detect space targets.

Detecting faint space targets is problematic in many wide-field surveillance systems. Given that the space targets are far away from the detector, they only cover a small number of pixels when imaged on the focal plane and appear as a low intensity point source. Thus, feature-based methods that perform well under the condition of a homogeneous background, such as threshold methods (Chang et al., 2007; Xu et al., 2013), template matching (Liu et al., 2013; Bal and Alam, 2005; Liu et al., 2012), high-pass filtering methods (Yang et al., 2004), morphological operators (Bai, 2013; Bai et al., 2009; Soni et al., 1993; Wei et al., 2018), Hessian matrix (Chae et al., 2002; Jiang et al., 2008), fail to detect space targets in the complex background. Many methods have been proposed to detect faint targets in optical images. Based on three-dimensional matched filtering, Reed et al. (1990) proposed a recursive detection method for space targets with known velocity. However, the detection performance of this algorithm is not satisfactory for targets with unknown velocities. Chu (1998) proposed a target detection algorithm that downscales 3D detection to 2D detection, called maximum value projection. Although the calculation cost is reduced, the detection accuracy of this method is reduced due to the velocity mismatch caused by the division of the velocity space (Chu, 1989).

To eliminate the impact of the velocity problem on the target detection probability, many methods were proposed. Yao et al. (2015) proposed a target detection method based on the maximum projection method, and estimated the target motion velocity by using time index and target centroid. Sun and Zhao (2013) and Sun et al. (2015) proposed a processing pipeline that can automatically detect objects. This method uses mathematical morphological filtering and median filtering to remove stars and noise and extract target positions. Kravchonok (2011) proposed a detection method based on optical flow, which detects targets by judging the change in the optical flow vector of the object. The Dynamic Programming Algorithm (DPA) solves the problem of faint target trajectory search by segmentation optimization, which was first proposed by Barniv and applied to small target detection (Barniv, 1985). This method combines the optimization principle with the ballistic integration principle, and transforms the problem of small space target detection into the problem of

* Corresponding author.
E-mail address: ciomp_d@126.com (X. Wang).

https://doi.org/10.1016/j.ascom.2020.100408
2213-1337/

finding the line with the largest cumulative value of gray. Tonissen and Evans (1996) eliminated the complex transfer function by taking the sum of the measurements as the optimal value function. The DPA is performed in an efficient manner, which is equivalent to exhaustive search for all possible target trajectories (Johnston and Krishnamurthy, 2000). The multistage hypothesis testing (MHT) method, proposed by Blostein and Huang (1991), is used to detect small and dim space targets. A large number of candidate trajectories form a tree structure lookup table. This method uses hypothesis testing to remove unverified trajectories at any time to achieve the purpose of reducing the amount of computing and storage. However, some obstacles still exist in these algorithms. Firstly, under the condition of a long exposure time, background noise increases, some stars image as streak-like sources, and the target trajectory may be nonlinear or discontinuous (points of space targets in the trajectories are missing because of the interference of random background noise or the covering of background stars); Secondly, the computational cost is high (especially in wide-field surveillance), the number of objects is numerous. These complicated situations bring difficulties to space target detection.

To overcome these obstacles, this paper presents a high detection probability and low computational cost target detection method named State Transition Multistage Hypothesis Testing (STMHT) method. Firstly, image preprocessing is performed to remove stars and noise. The improved adaptive threshold method is applied to eliminate the background. After analyzing the imaging characteristics of stars, noise, and space targets in the time index image, we propose an omnidirectional morphological filtering method to remove stars and noise. Compared with space or frequency domain filtering, omnidirectional morphological filtering has a lower computational cost. The intensities of the stars are estimated to further eliminate them from the maximum value projection image. Secondly, the relative inter frame motion distance can be used as the basis for predicting the valid state transition region in each image. We only need to search for targets in the valid state transition region rather than at every pixel in every image. Therefore, the space targets with different orbital altitudes and nonlinear trajectories can be effectively detected; and the computational cost is greatly saved. Thirdly, the state transition multistage hypothesis testing method is adopted to detect space targets. The multistage hypothesis testing criterion guarantees the detection probability of space targets with discontinuous trajectories.

The proposed method is not suitable for detecting space objects that move relatively slowly or rapidly respect to field stars, as well as objects that rotate rapidly. Our image is obtained in sidereal tracking mode and long exposure time. For objects with relatively slow speed, they will form short streaks with length comparable to width during optical observation, which will impact the prediction accuracy of the algorithm in the valid state transition stage. For objects with relatively fast speed, they have short pass duration, so they only appear in a few frames during shooting. Due to the limitation of the number of frames, the performance of the algorithm in the multistage hypothesis testing stage is affected. For long streaks of space objects with rapidly changing brightness, streak length in general is not a characteristic of the target's apparent velocity since the ends or any other part of the streak may fall below the detection threshold, which will impact the prediction accuracy of the algorithm in the valid state transition stage.

2. Image preprocessing

An optical image can be roughly divided into four components: the background, the star, the noise, and the space target. So it can be modeled as:

$$f(i,\ j,\ k) = B(i,\ j,\ k) + S(i,\ j,\ k) + T(i,\ j,\ k) + n(i,\ j,\ k) \qquad (1)$$

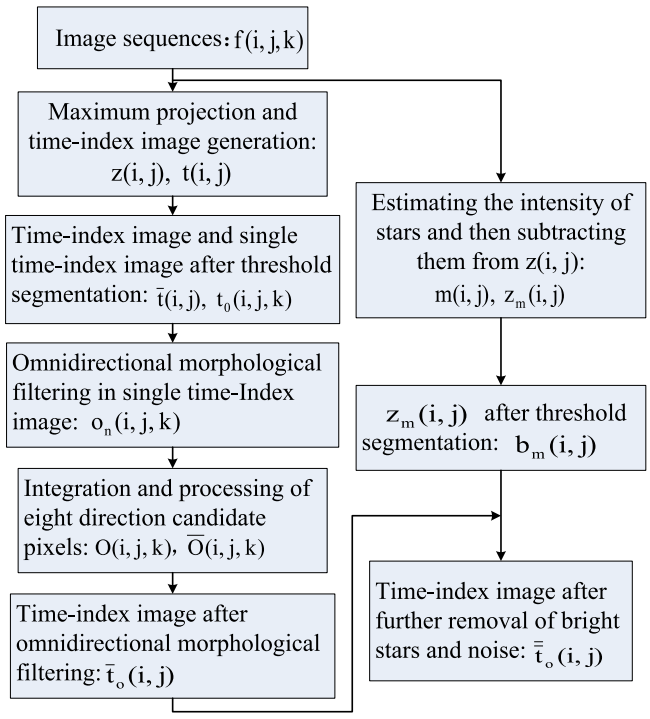

Fig. 1. Block diagram of the proposed image preprocessing method.

where f is an N × N optical image. (i, j) represents the integer space coordinates, k refers to the frame index of image sequence. f(i, j, k) represents the gray-scale value at coordinate (i, j). B(i, j, k) represents the background. S(i, j, k) and T(i, j, k) denote stars and space targets, respectively. The noise, n(i, j, k), is considered to contain two categories: one is the internal noise generated by the imaging system, and the other is the external noise which is generated by the external environment (Liu et al., 2017). The block diagram of the proposed image preprocessing method is shown in Fig. 1.

2.1. Principle of a time-index image

Chu (1998) proposed a target detection method called maximum value projection. If a frame set contains K frame images, the maximum value projection image can be obtained by the following equation:

$$z(i,\ j) = \max[f(i,\ j,\ k)],\ (1 \le k \le K) \qquad (2)$$

Where z(i, j) is the maximum value projection image (see Fig. 2(a)).

The time-index image t(i, j) can be obtained as follows:

$$z(i,\ j) = f(i,\ j,\ k) \quad \Longrightarrow \quad t(i,\ j) = k \qquad (3)$$

When the same gray value appears at the same coordinate in different images, the smaller frame index is to be recorded (see Fig. 2(b)). (The color bar in Fig. 2(b) only accepts integer values on the scale, and this principle applies to subsequent images of the same type.)

In order to effectively implement the proposed method, an improved adaptive threshold algorithm is applied to the maximum value projection image. Due to the interference of stars and space targets, the mean and standard deviation of the entire image are significantly higher than those of the noise. If the threshold calculated by the mean and standard deviation of the entire image is used to segment the image, the faint target will be

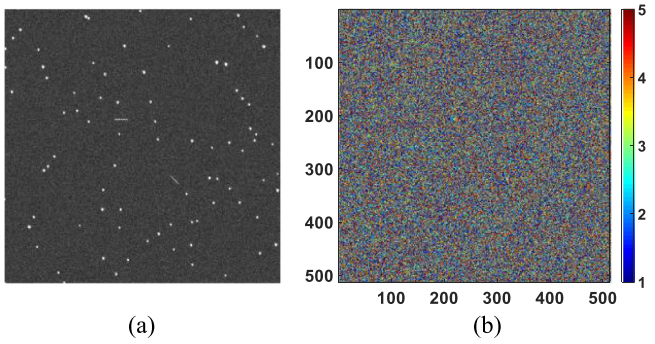

Fig. 2. (a) Example of the maximum projection of five sequential images. (b) Time-index image generated from (a).

incorrectly classified as the background. Therefore, an improved adaptive method based on row calculation, with the following steps, is proposed:

(1) The segmentation threshold is calculated as

$$\mathrm{Th_i} = \mu_\mathrm{i} + \alpha\sigma_\mathrm{i} \quad (1 \le \mathrm{i} \le \mathrm{N}) \tag{4}$$

where α is a coefficient, $\alpha = 1.5$ is selected to detect the space target with low SNR.

(2) The estimated mean and standard deviation of the i^{th} row of the image can be obtained by:

$$\mu_\mathrm{i} = \frac{1}{\mathrm{N}}\sum_{\mathrm{j}=1}^{\mathrm{N}} \bar{\mathrm{z}}(\mathrm{i},\ \mathrm{j}) \tag{5}$$

$$\sigma_\mathrm{i} = \sqrt{\frac{\sum_{\mathrm{j}=1}^{\mathrm{N}}(\bar{\mathrm{z}}(\mathrm{i},\ \mathrm{j}) - \mu_\mathrm{i})^2}{\mathrm{N}-1}} \tag{6}$$

where

$$\bar{\mathrm{z}}\,(\mathrm{i},\mathrm{j}) = \mathrm{z}\,(\mathrm{i},\mathrm{j}) \quad (\mathrm{i}=1) \tag{7}$$

$$\bar{\mathrm{z}}\,(\mathrm{i},\mathrm{j}) = \begin{cases} \mathrm{z}\,(\mathrm{i},\mathrm{j}) & \mathrm{z}\,(\mathrm{i},\mathrm{j}) < \mathrm{Th}_{\mathrm{i}-1} \\ \mathrm{Th}_{\mathrm{i}-1} & \mathrm{z}\,(\mathrm{i},\mathrm{j}) \ge \mathrm{Th}_{\mathrm{i}-1} \end{cases} (\mathrm{i} > 1) \tag{8}$$

(3) The mean and standard deviation usually stabilize at rows i = 3–5.

Compared with the adaptive threshold algorithm and the local adaptive threshold algorithm, the proposed algorithm has lower computational cost. The experiment was performed on the same dataset. The average running time of the adaptive threshold algorithm, the local adaptive threshold algorithm and the proposed algorithm are: 0.2988 s, 0.2011 s, 0.0141 s.

The binary image b(i, j) of z (i, j) is obtained as:

$$\mathrm{b(i,j)} = \begin{cases} 1 & \mathrm{z}\,(\mathrm{i},\ \mathrm{j}) \ge \mathrm{Th_i} \\ 0 & \mathrm{z}\,(\mathrm{i},\ \mathrm{j}) < \mathrm{Th_i} \end{cases} \tag{9}$$

The time-index image is given by:

$$\bar{\mathrm{t}}\,(\mathrm{i},\ \mathrm{j}) = \mathrm{t}\,(\mathrm{i},\ \mathrm{j})\,\mathrm{b(i,j)} \tag{10}$$

Fig. 3 shows the time-index image after threshold segmentation.

The single time-index image $\mathrm{t_0}\,(\mathrm{i},\ \mathrm{j},\ \mathrm{k})$ can be obtained as follows:

$$\begin{cases} \bar{\mathrm{t}}\,(\mathrm{i},\ \mathrm{j}) = \mathrm{k} & \Longrightarrow \quad \mathrm{t_0}\,(\mathrm{i},\ \mathrm{j},\ \mathrm{k}) = \mathrm{k} \\ \bar{\mathrm{t}}\,(\mathrm{i},\ \mathrm{j}) \ne \mathrm{k} & \Longrightarrow \quad \mathrm{t_0}\,(\mathrm{i},\ \mathrm{j},\ \mathrm{k}) = 0 \end{cases} \tag{11}$$

2.2. Omnidirectional morphological filtering

Under the conditions of a long exposure time and sidereal tracking mode, in the time index image, the space target is a

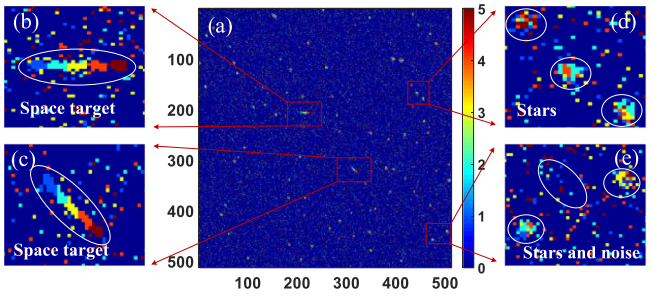

Fig. 3. (a) Time-index image after threshold segmentation. (b) (c) (d) (e) Space targets, stars, and noise in the time-index image.

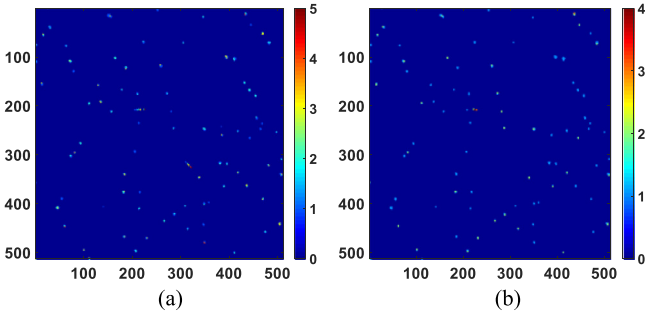

Fig. 4. Time-index image after traditional morphological filtering. (a) Symmetric 4-connected structuring element. (b) Symmetric 8-connected structuring element.

connected region with the same time index, while the discrete noise has a random isolated time index, and the stars are regions with different time indices (see Fig. 3, (b), (c), (d) and (e)), because the discrete noise is randomly distributed, and the intensities of the stars are not constant in different images. According to the difference between space targets, stars and noise, an omnidirectional morphological filtering is proposed to eliminate the stars and noise.

The traditional opening operation in morphological filtering can remove the region that is less than the structuring element. The morphological opening is defined as:

$$\mathrm{t}\,(\mathrm{i},\ \mathrm{j}) \circ \mathrm{b} = [\mathrm{t}\,(\mathrm{i},\ \mathrm{j}) \ominus \mathrm{b}] \oplus \mathrm{b} \tag{12}$$

where b is the structuring element, $\ominus$ refers to the erosion operation, $\oplus$ refers to the dilation operation. In the case of a long exposure time, the shapes of space targets in different moving directions are changing. The traditional opening operation only adopts a single structuring element (a symmetric 4- or 8-connected structuring element) to process the image, which will not produce the best results in detecting targets, removing stars and noise (see Fig. 4).

In this paper, we adopt the omnidirectional morphological opening in single time-index image, which is defined as follows:

$$\mathrm{o_n}\,(\mathrm{i},\ \mathrm{j},\ \mathrm{k}) = \mathrm{t_0}\,(\mathrm{i},\ \mathrm{j},\ \mathrm{k}) \circ \mathrm{b_n} = [\mathrm{t_0}\,(\mathrm{i},\ \mathrm{j},\ \mathrm{k}) \ominus \mathrm{b_n}] \oplus \mathrm{b_n} \tag{13}$$

Eight omnidirectional structuring elements $\mathrm{b_n}$ (n=1, 2,…,8) are designed and two-point clusters are selected to extract the space targets with low SNR, the dimensions of these structuring elements are 3×3 (see Fig. 5).

Each $\mathrm{o_n}\,(\mathrm{i},\ \mathrm{j},\ \mathrm{k})$ may contain candidate space targets distributed in the detection direction, so we add these eight $\mathrm{o_n}\,(\mathrm{i},\ \mathrm{j},\ \mathrm{k})$ together to form a large $\mathrm{O}\,(\mathrm{i},\ \mathrm{j},\ \mathrm{k})$, which is calculated as follows:

$$\mathrm{O}\,(\mathrm{i},\ \mathrm{j},\ \mathrm{k}) = \mathrm{o_1}\,(\mathrm{i},\ \mathrm{j},\ \mathrm{k}) + \mathrm{o_2}\,(\mathrm{i},\ \mathrm{j},\ \mathrm{k}) + \cdots + \mathrm{o_8}\,(\mathrm{i},\ \mathrm{j},\ \mathrm{k}) \tag{14}$$

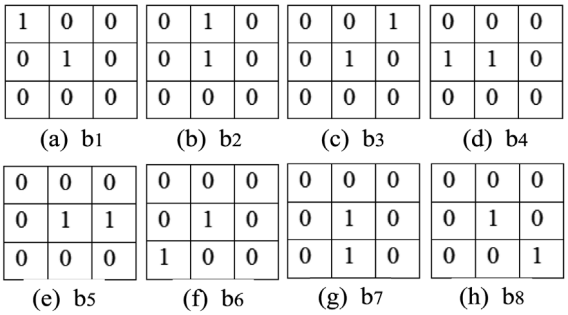

Fig. 5. Eight-direction structuring elements ($b_1 \rightarrow 135°, b_2 \rightarrow 90°, b_3 \rightarrow 45°, b_4 \rightarrow 180°, b_5 \rightarrow 0°, b_6 \rightarrow 225°, b_7 \rightarrow 270°, b_8 \rightarrow 315°$).

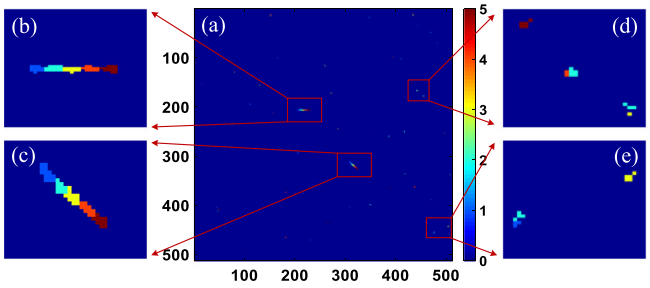

Fig. 6. Time-index image after omnidirectional morphological filtering.

The adaptive threshold is used to deal with the above O (i, j, k), and then the candidate space targets are extracted. In this paper, 4k is selected to detect the space targets with low SNR.

$$\overline{O}(i,\ j,\ k) = \begin{cases} k & O(i,\ j,\ k) \geq 4k \\ 0 & O(i,\ j,\ k) < 4k \end{cases} \tag{15}$$

where k refers to the frame index of image sequence.

The time-index image after omnidirectional morphological filtering is:

$$\bar{t}_o(i,\ j) = \overline{O}(i,\ j,\ 1) + \overline{O}(i,\ j,\ 2) + \cdots + \overline{O}(i,\ j,\ K) \tag{16}$$

The result is shown in Fig. 6.

2.3. Bright star removal

Although discrete noise is randomly distributed, and the intensities of the stars are not constant in different images, they may still form connected regions with the same time index as space targets. Therefore, the stars and noise cannot be removed completely by omnidirectional morphological filtering alone (see Fig. 6). Due to their large number of pixels and high intensities, bright stars are more likely to stay in the time-index image. Estimating the intensities of the stars and then subtracting them from the maximum value projection image is one way to remove stars. The median value projection in a frame set is used to estimate the intensity of stars. The median value projection image can be obtained by computing the median value of K images at each pixel (i, j):

$$m(i,\ j) = \text{median}\ [\ f(i,\ j,\ k)], (1 \leq k \leq K) \tag{17}$$

where m (i, j) is the median value projection image, in which the stars and noise are still present, while the space targets are absent. The image after removing the stars and noise is represented as follows:

$$z_m(i,\ j) = z(i,\ j) - m(i,\ j) \tag{18}$$

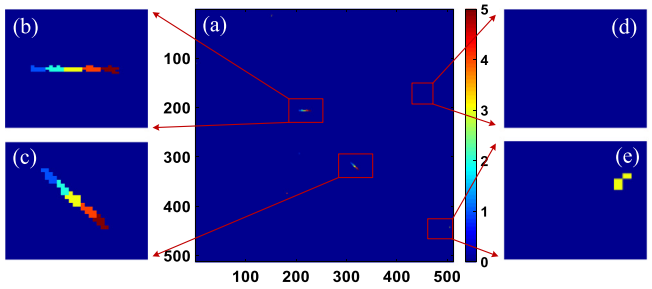

Fig. 7. Time-index image after further removal of bright stars.

However, as discussed before, the intensities of the stars are not constant; there will be some residual background in the above image. Therefore, the threshold method is adopted again to remove the residual background, and the binary image $b_m(i, j)$ of $z_m(i, j)$ is obtained.

After the bright stars and noise are further removed, the time-index image is given by:

$$\bar{\bar{t}}_o(i,\ j) = \bar{t}_o(i,\ j)\, b_m(i, j) \tag{19}$$

The result is shown in Fig. 7, which demonstrates that most of the stars have been removed, leaving only candidate point targets and a few false alarms in the time-index image.

3. Space target detection

3.1. Valid state transitions

Kouprianov (2015) proposed a space debris detection pipeline method, which uses some natural criteria (residuals of the model path, the object's velocity and the curvature of its path) to quickly cut the search tree, discarding candidate trajectories that do not correspond to any real objects. The principle is to extract a set of trajectories that can be approximated by linear or quadratic motion models. Due to the uniqueness of the conditions set in this paper, more information can be used to improve and simplify the above method, but the generality of the method is reduced.

Under the conditions of a sidereal tracking mode and long exposure time, the space target is seen as a streak-like source in random direction. In this situation, the space target makes an apparent motion in the inter-frame (See Fig. 8). When the exposure time t_e and the time interval t_s between two adjacent frames are known, the relative inter frame motion distance is obtained as follows:

$$d_{x(k,k+1)} = \frac{t_e + t_s}{t_e} d_{ex} \tag{20}$$

$$d_{y(k,k+1)} = \frac{t_e + t_s}{t_e} d_{ey} \tag{21}$$

where d_{ex}, d_{ey} are the streak length components of the target in the horizontal and vertical directions, respectively. $d_{x(k,k+1)}$, $d_{y(k,k+1)}$ are the relative inter frame motion distance components in the horizontal and vertical directions, respectively, which can be used as the basis for selecting the transfer region.

Because the detector used to capture the star background image is discrete. In addition, the requirement for the accuracy of target centroid positioning will be reduced if the target motion is predicted in the discrete state space. Therefore, the successive space is quantized as $\Delta \times \Delta$ cells, whose size is equal to the measurement resolution unit. The relationship between continuous and discrete states is as follows:

$$\begin{cases} x(k) \in [(\bar{x} - 1)\,\Delta, \bar{x}\Delta) \\ y(k) \in [(\bar{y} - 1)\,\Delta, \bar{y}\Delta) \end{cases} \tag{22}$$

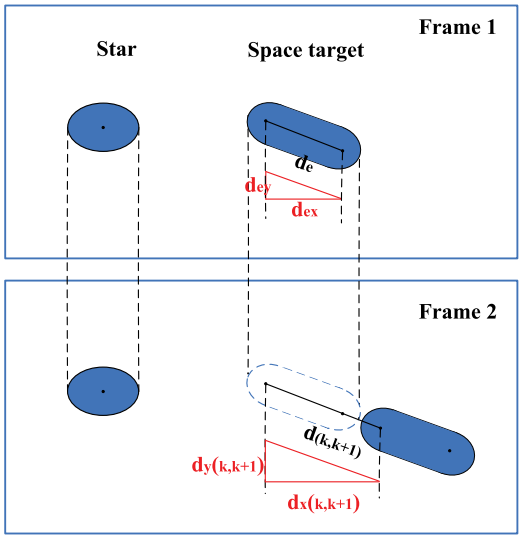

Fig. 8. Motion model for space target and star in the inter-frame during long exposure time.

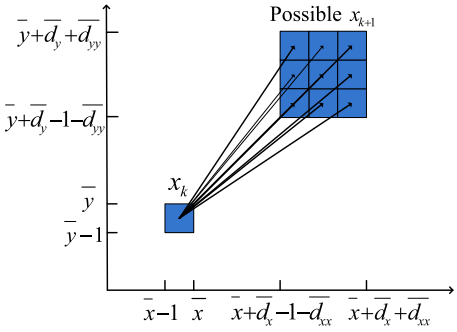

Fig. 9. Valid state transitions.

where $\bar{x}$ and $\bar{y}$ represent discrete coordinates in quantized pixel space.

The adaptive valid state transitions of the target in the next frame are:

$$\begin{cases} x(k+1) \in [(\bar{x}+\bar{d}_x-1-\bar{d}_{xx})\,\Delta, (\bar{x}+\bar{d}_x+\bar{d}_{xx})\,\Delta) \\ y(k+1) \in [(\bar{y}+\bar{d}_y-1-\bar{d}_{yy})\,\Delta, (\bar{y}+\bar{d}_y+\bar{d}_{yy})\,\Delta) \end{cases} \tag{23}$$

where $\bar{d}_x$, $\bar{d}_y$ are discretized relative interframe motion distances. The discrete state expansions $\bar{d}_{xx}$ and $\bar{d}_{yy}$ are introduced to ensure the detection probability of targets with nonlinear trajectories. The value of $\bar{d}_{xx}$ and $\bar{d}_{yy}$ are $\lceil 0.5\bar{d}_x \rceil$ and $\lceil 0.5\bar{d}_y \rceil$, respectively. The outer parentheses indicate rounding up.

This method only needs to search for space targets in the valid state transition region of each frame (see Fig. 9, $\bar{d}_{xx} = 1$, $\bar{d}_{yy} = 1$). On the one hand, space targets with different orbital altitudes and nonlinear trajectories can be effectively detected; on the other hand, computational cost is greatly saved. These are the advantages of this method.

3.2. State transition multistage hypothesis testing

After image preprocessing and valid state transition, the state transition multistage hypothesis testing (STMHT) method proposed in this paper is performed. Five images are used at a time to detect space targets. The proposed STMHT method is initiated with the candidate space targets with frame index 1 in time-index image as the starting points to search for the trajectory

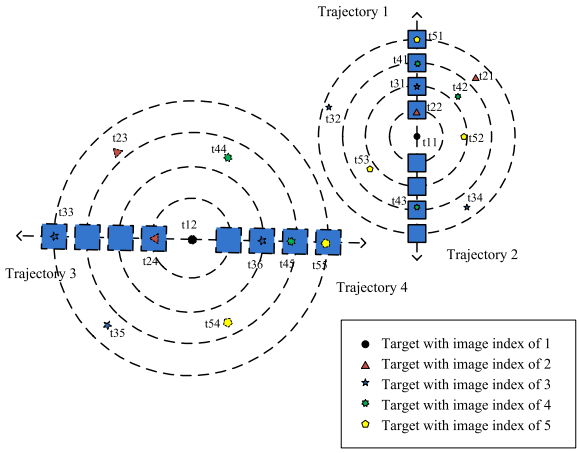

Fig. 10. STMHT search. This diagram only shows some typical candidate trajectories.

points with frame indices 2, 3, 4, and 5 in the valid state transition region. Because the streak length of target in a single frame image is used to predict the valid state transition region, the moving direction cannot be determined. In other words, for the same target, we should carry out forward and reverse bidirectional detection (see Fig. 10). The blue rectangle represents the valid state transition region, and the targets appearing in the rectangle are recorded in Table 1. The columns in Table 1 indicate the candidate trajectory points t_{kk_1}, where k refers to the frame index number, k_1 refers to the ordinal number of the candidate target among all the candidate targets with frame index k. The total number of frames in which the target appears in the valid state transition region of the candidate trajectory starting from target t_{kk_1} is denoted by N.

In order to balance the target detection probability and calculation cost, two stages of STMHT are proposed.

First stage of STMHT: the first stage of STMHT uses the number of frames that the target appears in a candidate trajectory.

$$N = \sum_{k=1}^{K} n_k \begin{cases} \le C_1 & \text{choose } T_0 \\ \ge C_2 & \text{choose } T_1 \\ \in (C_1, C_2) & \text{undecided} \end{cases} \tag{24}$$

where $\sum_{k=1}^{K} n_k$ refers to the number of frames in which the target appears in the valid state transition region of the candidate trajectory. If a target is detected in the valid state transition region, the value of n_k is equal to 1, otherwise n_k is equal to 0. C_1 and C_2 are determined by the number of images in the frameset, K. T_1 indicates that the candidate target is a real space target, T_0 indicates that the candidate target is not a real space target. In this study, $K = 5$, $C_1 = 2$, $C_2 = 4$.

Second stage of STMHT: For the undecided targets, increase the number of frames used for detection, as follows:

$$N = \sum_{k=1}^{K_2} n_k \begin{cases} < C_3 & \text{choose } T_0 \\ \ge C_3 & \text{choose } T_1 \end{cases} \tag{25}$$

where $K_2 = 2 \times K = 10$, $C_3 = 6$.

According to the determination conditions, the candidate trajectory 1 and candidate trajectory 4 in Table 1 are respectively determined as the true trajectories for t_{11} and t_{12} in Fig. 10. However, the space target may not be detected in the first frame, thus the algorithm should be executed starting from frame index 2 and frame index 3 (both the first and second targets are lost) when the number of frame set is 5. The multistage hypothesis

Table 1
Candidate trajectories of t_{11} and t_{12} in the time-index image.

Candidate trajectories	1	2	3	4
First frame image	t11	t11	t12	t12
Second frame image	t22	0	t24	0
Third frame image	t31	0	0	t36
Fourth frame image	t41	t43	0	t45
Fifth frame image	t51	0	0	t55
Total number N	5	2	2	4

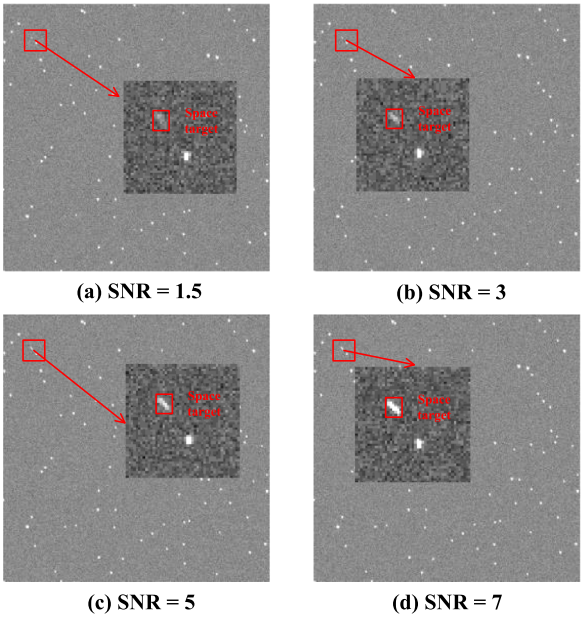

Fig. 11. Simulated space targets with different SNR.

testing criterion guarantees the detection probability of space targets with discontinuous trajectories.

Computational cost: In the original MHT method, we need to search for space targets at every pixel in every sequence image. In the experiment, there are N_{sets} frame sets, and each set has K images with M × N pixels. Thus the total computational cost of MHT is proportional to MN^{K_0}, where $K_0 = N_{sets}K$. In the STMHT method, if the maximum number of candidate space targets (including false alarms) in all K_0 images is N_{max}, the size of the valid state transition region is $(2\overline{d_{xx}}+1)(2\overline{d_{yy}}+1)$, then $N_{max} \ll MN$, $[(2\overline{d_{xx}}+1)(2\overline{d_{yy}}+1)] \ll MN$. The maximum computational cost of the STMHT method is proportional to:

$$2N_{sets}N_{max}(K-1)[(2\overline{d_{xx}}+1)(2\overline{d_{yy}}+1)] \ll MN^{K_0} \tag{26}$$

In short, the computation cost of the STMHT method is considerably lower than that of the MHT method.

4. Experiments

Under the conditions of a sidereal tracking mode and long exposure time, the star appears as a point source and the space target is seen as a streak-like source. The image size is 1024 × 1024 pixels. For clearer display, only 512 × 512 pixels are clipped for demonstration. The method is programmed using Matlab, and the PC specifications include an i7-6700M CPU (3.40 GHz), 8 GB memory.

According to the Tycho-2 catalogue, the intensity and position of background stars are simulated. The targets with different motion angles and streak lengths (ranging from 3 to 8) are added to 800 star images. These images are divided into four sets, and

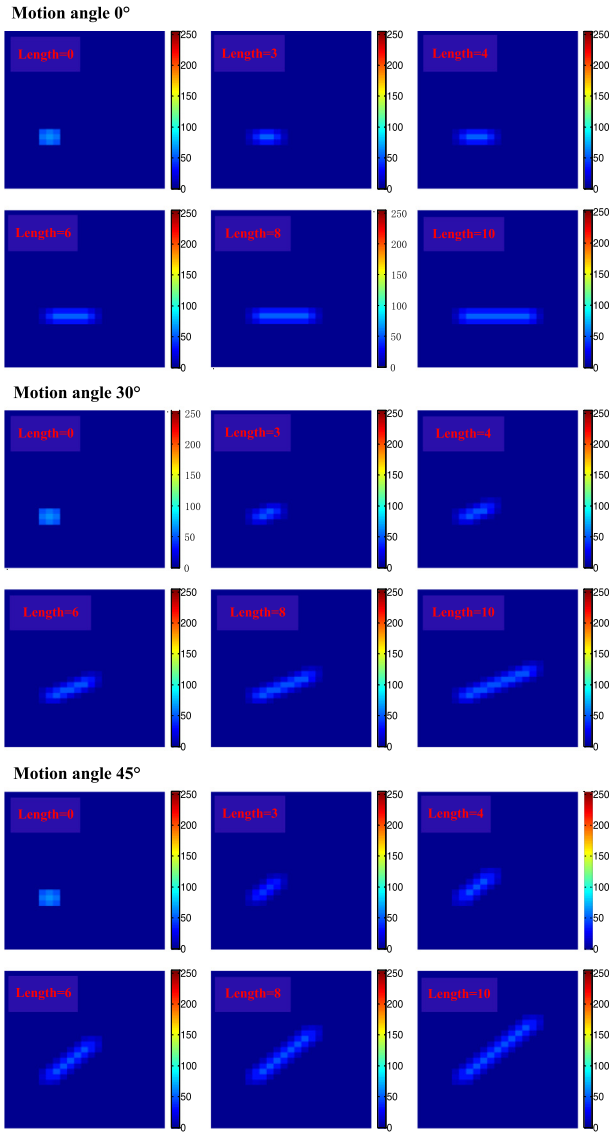

Fig. 12. Simulated space targets with different motion angles and streak lengths.

the SNRs of the simulated targets in each set are 7, 5, 3, and 1.5. The simulated space targets with different SNRs, motion angles and streak lengths are shown in Figs. 11 and 12, respectively.

To validate the detection performance of the STMHT method, two indicators of detection probability (P_d) and false alarm rate (FAR) are introduced. The P_d and FAR are calculated based on the true target (TT), missing target (MT), and false target (FT).

$$P_d = \frac{TT}{TT + MT} \tag{27}$$

$$FAR = \frac{FT}{FT + TT + MT} \tag{28}$$

where TT, MT, and FT represent the numbers of detected space targets, the true space targets that missed detection, and false alarms that are misidentified as space targets, respectively.

4.1. Space target detection using STMHT

In this section, we analyzed the STMHT algorithm in terms of detection and false alarm rejection. The preliminary results before using the STMHT method are shown in Fig. 13, which represent

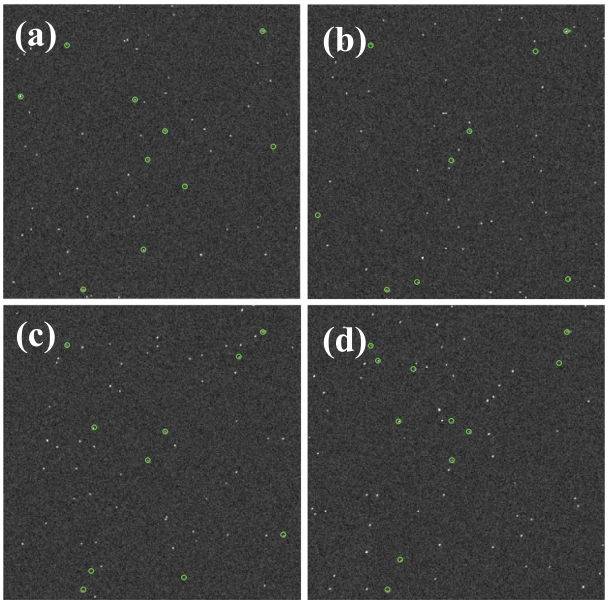

Fig. 13. Space target detection results before using the STMHT.

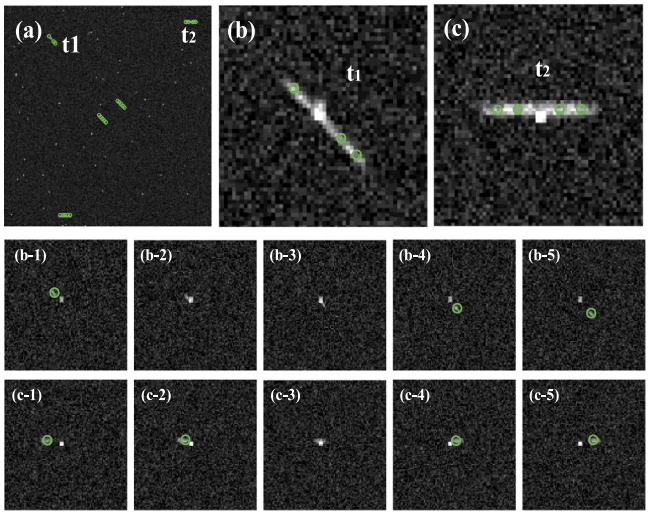

Fig. 14. (a) Detection results, (frames 1–5). (b), (c) Enlarged area of the targets t_1 and t_2. (b-1) to (b-5), (c-1) to (c-5) detection results of targets t_1 and t_2 in five frames.

the detection results under four different star backgrounds, and the green circles in the image represent the detected candidate points. In different backgrounds, false alarms generated by stars and noise with different positions have no continuous trajectory, which can be eliminated through the STMHT algorithm.

Then, STMHT algorithm is used to further detect candidate points. Fig. 14 shows the detection results and the enlarged regions of the targets t_1 and t_2, respectively. It can be seen that the false alarms have been removed. The green circles in the image represent the detected space targets and undecided targets. In frame set 2, the undecided target is checked. Undecided target t_1 has eight trajectory points in frame sets 1 and 2; therefore, it is confirmed as a real space target. Fig. 15 shows the detection results of the discontinuous trajectories. All five simulated space targets are detected successfully.

The nonlinear situations of the target trajectories are further tested. The detection results are shown in Fig. 16.

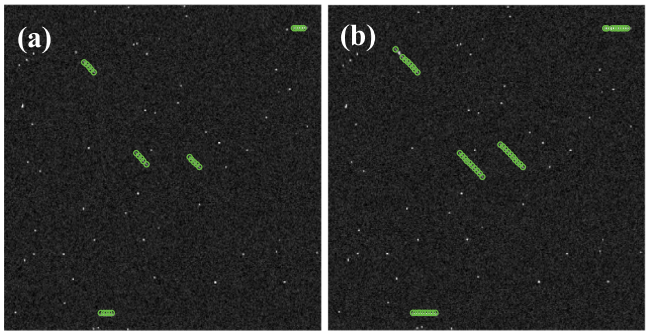

Fig. 15. Space target detection results of the discontinuous trajectories. (a) Frame set 2 (frames 6–10), (b) Frame sets 1–2 (frames 1–10).

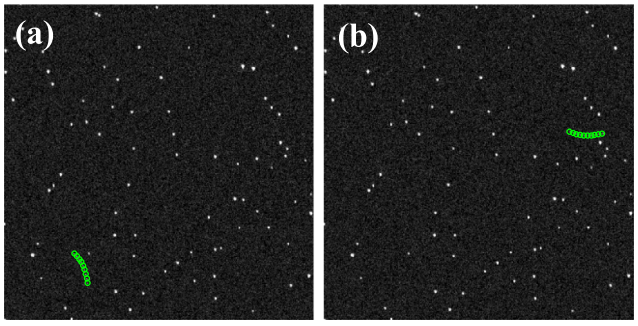

Fig. 16. Space target detection results of the nonlinear trajectories.

Table 2
Statistical results of simulated space target detection.

Method	Detection probability (%)				False alarm rate (%)			
	SNR=7	SNR=5	SNR=3	SNR=1.5	SNR=7	SNR=5	SNR=3	SNR=1.5
MHT	97.7	96.3	91.5	77.1	2.2	2.6	3.9	20.7
NTH	98.6	97.6	96.5	80.7	4.5	5.2	18.9	63.3
IMTI	98.5	97.1	95.8	82.4	0.6	0.9	2.1	16.3
Ours	100	100	100	92.1	0	0	0	6.5

We further verified the detection probability and false alarm rate of the STMHT algorithm, and the statistical results are shown in Table 2.

To prove the advantages of the proposed method, we compared it with the multistage hypothesis testing method (MHT) (Blostein and Huang, 1991), the new top-hat method (NTH) (Bai and Zhou, 2010), and the improved maximum value projection method (IMTI) (Yao et al., 2015) under the same frame sets. When the SNR is higher than or equal to 3, the STMHT algorithm can successfully detect all the space targets without any false alarms. Even when the SNR is as low as 1.5, the detection probability is still higher than 90%. As shown in Table 2, compared with other methods, the proposed method has performed better in terms of detection and false-alarm rejection between frame sets in the SNR range of 7 to 1.5.

4.2. Real space target detection

To evaluate its performance in detection and false-alarm rejection, the STMHT algorithm was further tested on a real image sequence of 500 images collected by the telescope equipped with a CMOS sensor. The exposure time is 3 s, the field of view $10^\circ \times 10^\circ$. These real images have 10K $\times$ 10K imaging pixels, 12 bits of grayscale. They are captured on the ground in the sidereal tracking mode. The telescope is installed on a turntable which can counteract the rotation speed of the earth. Space targets appear as

Table 3
Statistical results of real space target detection.

Method	Detection probability	False alarm rate	Running time
MHT	86.9%	16.2%	35.81 s
NTH	91.6%	71.4%	0.52 s
IMTI	90.5%	13.6%	2.59 s
Ours	98.5%	5.1%	1.58 s

streak-like objects. Some stars also appear as streak-like objects due to the influence of platform vibration. The most intuitive way to determine the ground truth is through the eyes, so the test results in Table 3 are for reference, and the results in Table 2 are more accurate.

To validate the advantages of the STMHT method, MHT (Blostein and Huang, 1991), NTH (Bai and Zhou, 2010), and IMTI (Yao et al., 2015) are used to detect the same real image sequences. Table 3 shows the statistical results of different methods.

The MHT method does not use the prior information of moving target, thus the detection is performed at every pixel in every sequence image; in addition, the candidate trajectories will increase rapidly when the number of test stages increases, resulting in a large computational cost. It can be seen from the statistical results that the NTH method is simple and fast. However, under the conditions of a long exposure time and wide field of view, the detection result of the NTH method is affected by the streak-like background stars, resulting in an extremely high false alarm rate. The IMTI method is also affected by the streak-like background stars and noise, which has a high false alarm rate; and in the target detection stage, at least 15 images are needed; therefore, 15 test images should be stored until the detection process is completed.

The STMHT method overcomes the shortcomings of the above method, including a large computational cost, a high false alarm rate and a low detection probability in the case of wide-field surveillance and long exposure time.

5. Conclusions

In this paper, we propose a methodology for detecting space targets in wide-field surveillance. Under the conditions of a long exposure time and wide field of view, some stars image as streak-like sources, and there are many resident objects in the field of view. The proposed omnidirectional morphological filtering method can effectively eliminate stars and noise at a low computational load. After removing stars and noise, the valid state transition region in each image is predicted. The relative inter frame motion distance can overcome the obstacles for the detection of targets with different orbital altitudes, and the discrete state expansion can overcome the obstacles for the detection of targets with nonlinear trajectories. Finally, the STMHT method is adopted to detect space targets. The multistage hypothesis testing criterion guarantees the detection probability of targets with discontinuous trajectories. As demonstrated by the experimental results in simulated image sequences and real image sequences, the STMHT method overcomes the obstacles of space target detection in wide-field surveillance, and has a high detection probability and low computational cost.

Funding

Strategic Priority Research Program of Chinese Academy of Sciences (Grant No. XDA17010205).

Declaration of competing interest

The authors declare that they have no known competing financial interests or personal relationships that could have appeared to influence the work reported in this paper.

References

Bai, X., 2013. Morphological operator for infrared dim small target enhancement using dilation and erosion through structuring element construction. Optik 124 (23), 6163–6166. doi:10.1016/j.ijleo.2013.04.098.

Bai, X., Zhou, F., 2010. Analysis of new top-hat transformation and the application for infrared dim small target detection. Pattern Recognit. 43 (6), 2145–2156. doi:10.1016/j.patcog.2009.12.023.

Bai, X., Zhou, F., Xie, Y., Jin, T., 2009. Enhanced detect ability of point target using adaptive morphological clutter elimination by importing the properties of the target region. Signal Process. 89 (10), 1973–1989. doi:10.1016/j.sigpro.2009.03.036.

Bal, A., Alam, M.S., 2005. Automatic target tracking in FLIR image sequences using intensity variation function and template modeling. IEEE Trans. Instrum. Meas. 54 (5), 1846–1852. doi:10.1109/TIM.2005.855090.

Barniv, Y., 1985. Dynamic programming solution for detecting dim moving targets. IEEE Trans. Aerosp. Electron. Syst. 21 (1), 144–156. doi:10.1109/TAES.1985.310548.

Blostein, S.D., Huang, T.S., 1991. Detecting small, moving objects in image sequences using sequential hypothesis testing. IEEE Trans. Signal Process. 39 (7), 1611–1629.

Castronuovo, M.M., 2011. Active space debris removal-A preliminary mission analysis and design. Acta Astronaut. 69 (9), 848–859. doi:10.1016/j.actaastro.2011.04.017.

Chae, S.W., Kwon, K.Y., Lee, T.S., 2002. An optimal design system for spot welding locations. Finite Elements Anal. Des. 38 (3), 277–294. doi:10.1016/S0168-874X(01)00064-6.

Chang, Y.K., Kang, S.J., Lee, B.H., 2007. High-accuracy image centroiding algorithm for CMOS-based digital sun sensors. IEEE Sensors 32, 9–336. doi:10.1109/ICSENS.2007.4388403.

Chu, P.L., 1989. Efficient Detection of Small Moving Objects. MIT Lincoln Laboratory Technical Report, pp. 35–41.

Chu, P.L., 1998. Optimal projection for multidimensional signal detection. IEEE Trans. Acoust. Speech Signal Process. 36 (5), 775–786. doi:10.1109/29.1587.

Esmiller, B., Jacquelard, C., Eckel, H., Wnuk, E., 2014. Space debris removal by ground-based lasers: main conclusions of the European project: CLEANSPACE. Appl. Opt. 53 (31), 145–154. doi:10.1364/AO.53.000I45.

Jiang, J., Deng, J., Zhang, G., Zhou, F., 2008. Real-time implementation of light stripe center extraction. Opt. Tech. 34, 170–173.

Johnston, L.A., Krishnamurthy, V., 2000. Performance analysis of a track before detect dynamic programming algorithm. In: IEEE International Conference on Acoustics, Speech, and Signal Processing, Istanbul, Vol. 38, No. 1. pp. 49–52. doi:10.1109/7.993242.

Kouprianov, V., 2015. ISON space debris detection pipeline: Recent developments. In: International Astronautical Congress. pp. 1–7.

Kravchonok, A., 2011. Detection of moving objects in video sequences by the computation of optical flow based on region growing. Pattern Recognit. Image Anal. 21, 283–286.

Liu, R., Li, X., Han, L., Meng, J., 2013. Track infrared point targets based on projection coefficient templates and non-linear correlation combined with Kalman prediction. Infrared Phys. Technol. 57, 68–75. doi:10.1016/j.infrared.2012.12.011.

Liu, R., Lu, Y., Gong, C., Liu, Y., 2012. Infrared point target detection with improved template matching. Infrared Phys. Technol. 55 (4), 380–387. doi:10.1016/j.infrared.2012.01.006.

Liu, R., Wang, D., Zhou, D., Jia, P., 2017. Point target detection based on multiscale morphological filtering and an energy concentration criterion. Appl. Opt. 6796–6805. doi:10.1364/AO.56.006796.

Nunez, J., Nunez, A., Montojo, F.J., Condominas, M., 2015. Improving space debris detection in GEO ring using image deconvolution. Adv. Space Res. 56 (2), 218–228. doi:10.1016/j.asr.2015.04.006.

Reed, I.S., Gagliardi, R.M., Stotts, L.B., 1990. A recursive moving-target-indication algorithm for optical image sequences. IEEE Trans. Aerosp. Electron. Syst. 26 (3), 434–440. doi:10.1109/7.106120.

Soni, T., Zeidler, J.R., Ku, W.H., 1993. Performance evaluation of 2-D adaptive prediction filters for detection of small objects in image data. IEEE Trans. Image Process. 2 (3), 327–340. doi:10.1109/83.236534.

Sun, R., Zhan, J., Zhao, C., Zhang, X., 2015. Algorithms and applications for detecting faint space debris in GEO. Acta Astronaut. 110, 9–17. doi:10.1016/j.actaastro.2015.01.001.

Sun, R., Zhao, C., 2013. A new source extraction algorithm for optical space debris observation. Res. Astron. Astrophys. 13, 604–614.

Tonissen, S.M., Evans, R.J., 1996. Performance of dynamic programming techniques for track-before-detect. IEEE Trans. Aerosp. Electron. Syst. 32 (4), 1440–1451. doi:10.1109/7.543865.

Wei, M., Xing, F., You, Z., 2018. A real-time detection and positioning method for small and weak targets using a 1D morphology-based approach in 2D images. Light: Sci. Appl. 7.

Wirnsberger, H., Baur, O., Kirchner, G., 2015. Space debris orbit prediction errors using bi-static laser observations. Case study: ENVISAT. Adv. Space Res. 55 (11), 2607–2615. doi:10.1016/j.asr.2015.02.018.

Xu, W., Li, Q., Feng, H.J., Xu, Z.H., Chen, Y.T., 2013. A novel star image thresholding method for effective segmentation and centoid statistics. Optik 124 (20), 4673–4677. doi:10.1016/j.ijleo.2013.01.067.

Yang, L., Yang, J., Yang, K., 2004. Adaptive detection for infrared small target under sea-sky complex background. Electron. Lett. 40 (17), 1083–1085. doi:10.1049/el:20045204.

Yao, D., Wen, D., Xue, J., Chen, Z., Wen, Y., et al., 2015. Maximum projection and velocity estimation algorithm for small moving target detection in space surveillance. Image Process. Anal. 9675, doi:10.1117/12.2202360.